

AN INVESTIGATION OF ANOMALIES IN THE ARTIST SEA ICE CONCENTRATION ALGORITHM

Jessica M. Wiedemeier¹ and Valentin S. Ludwig²

¹School of Meteorology at the University of Oklahoma
Norman, Oklahoma, USA

²Institute of Environmental Physics at the University of Bremen
Bremen, Germany

ABSTRACT

This study evaluates the accuracy of the ARTIST Sea Ice algorithm over land-fast ice. The algorithm was found to have underestimations above 30% in some cases by comparison to optical images from the Landsat satellite and MODIS sensors. Several potential causes of these underestimations are entirely or partially disproved, including temperature changes, radiative flux, and atmospheric interference. Others lacked sufficient data to analyze, including salinity, snow characteristics, and surface roughness. Some potential causes lack sufficient data for analysis. Aside from these, many common error sources are eliminated as potential causes; however, the reason for the anomalies remains unclear.

1. INTRODUCTION

The ARTIST (Arctic Radiation and Turbulence Interaction Study) Sea Ice (ASI) algorithm generates 6.25 km resolution gridded sea ice concentration (C_{ice}) maps using passive microwave satellite data at 89 GHz. These maps can be used in climate studies, navigational chart production, and arctic biology research. Because of the use of the 89 GHz channel, the ASI algorithm gives resolutions almost 4 times as fine as the commonly-used NASA Team and Bootstrap algorithms (Spren et al. 2008, Kalescke et al. 2001). Additionally, it produces more accurate estimates of sea ice extent than other sea ice concentration algorithms and provides information closer to the coast than other widely-used algorithms due to its small footprint.

This study utilizes both passive microwave and optical data. Passive microwave data is important in remote sensing

because it is not dependent on sunlight. It is also relatively unaffected by clouds, although they can have some effect at 89 GHz.

Optical data, on the other hand, is simple to understand and has very high resolution of up to 10 m. However, it can be difficult to differentiate clouds, snow, and ice, and data is only available during the day (Wiebe 2007). This means that its availability in polar regions, where night can last for several months and days are often cloudy, is quite sparse. Still, it is often used as ground-truth because of the lack of error sources and ease of interpretation.

Recently, several areas where the ASI algorithm significantly underestimates sea ice concentration became apparent in comparison to 30 m-resolution optical Landsat 8 imagery (Example Figure 1.0.1). These anomalies persist over the course of at least several years, though their intensities and locations vary. The 2014-2015 season is analyzed in this study as a representative year with a variety of

Corresponding author address: Jessica Wiedemeier,
School of Meteorology at the University of Oklahoma.
Address: 240 Granite Lane, Austin, Texas, 78737.
Email: Jessica.M.Wiedemeier-1@ou.edu.

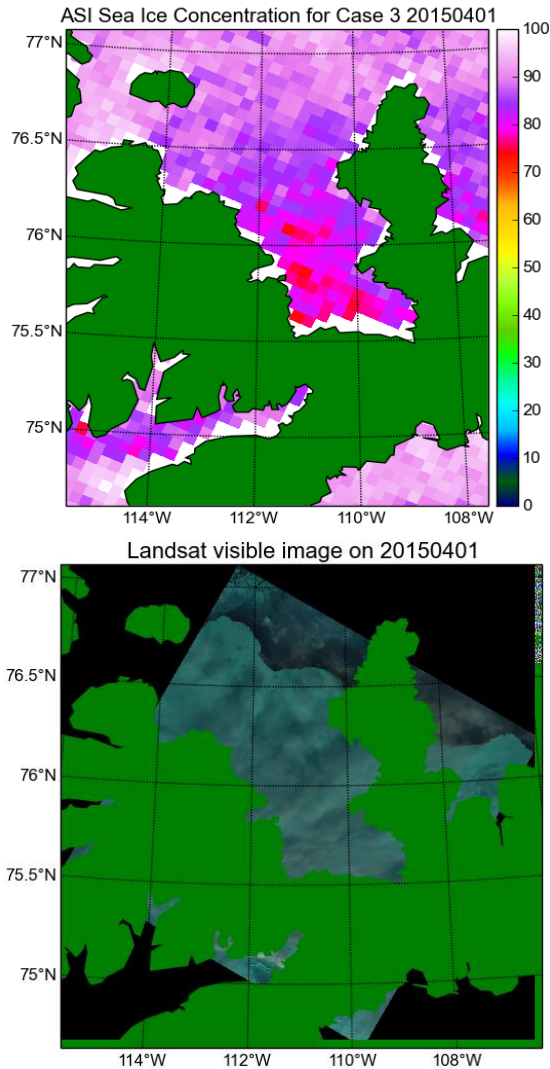


Figure 1.0.1: ASI concentration (top) showing underestimation in the bay and Landsat high-resolution optical image (bottom) showing a large sheet of fast ice in Hecla and Griper Bay on April 1st, 2015.

data products available. This study seeks the answers to two questions: What *could* cause such anomalies and what *does* cause these particular underestimations?

1.1 The Cases

This study investigates the ASI concentration reported for ten cases of land-fast ice, i.e., ice that is attached to a landmass,

in the Northern Hemisphere. Their locations are shown in Figure 1.1.2.

Significant anomalies (over 10% error) are present in six cases, while the ASI algorithm performs well in four cases (Table 1.1.1). This study considers errors consistently below 10% to be minor because, while small errors are common and could have many causes, the large errors this study investigates likely share a cause. The 10% threshold is a rough estimate – it is possible that whatever causes the larger error also causes the smaller errors, but would be more difficult to isolate where its impact is less significant.

Note that the proportions of good and bad cases are not meant to represent the performance of the ASI algorithm overall. Cases with extreme amounts of water vapor present were excluded from this study. Some water vapor is present in all cases and could account for some of the less significant anomalies, such as those in cases 7 and 10. Images of the ASI algorithm output and corresponding Landsat or MODIS visible imagery for selected dates can be found in Appendix A.

1.2 Physical Basis

Brightness temperature is the product of an object's temperature and emissivity (ϵ). ϵ is the ratio of emitted radiation to radiation emitted by a blackbody of the same temperature. Because of radiation from other objects (such as the atmosphere), emitted radiation in this calculation includes reflected radiation. When radiation encounters an interface between two mediums with different refractive indices, it can become polarized according to the Fresnel equations as more of one directional component of the radiation is transmitted and more of the other is reflected. The polarization is also dependent on the angle of incidence; at the Brewster angle (about 53° for a water-air interface), all of the

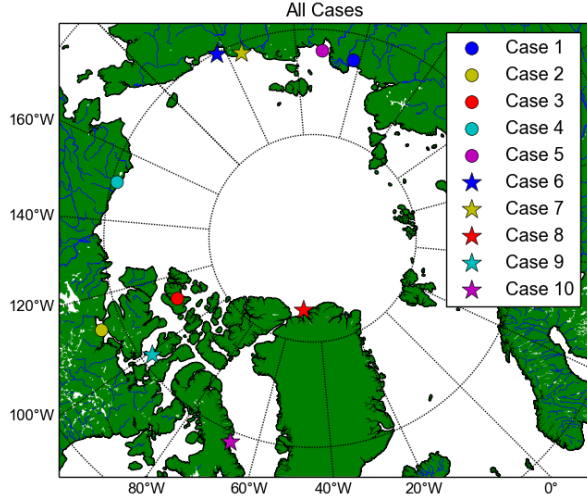


Figure 1.1.2: Overview of locations of cases investigated. The case numbers listed correspond with those used throughout the paper.

vertical polarization is transmitted. The AMSR-2 sensor uses an incidence angle of 55° , so brightness temperature from water used in the ASI algorithm is highly polarized. Vertical and horizontal polarizations of brightness temperature are denoted by $T_{B,V}$ and $T_{B,H}$, respectively. The polarization difference will be defined as

$$P = T_{B,V} - T_{B,H}. \quad (1)$$

For this algorithm, it is important to note that radiation emitted from water is more strongly polarized than that emitted from ice. Snow, which is found on ice in most cases, further lowers the polarization difference of brightness temperature from ice as it scatters the radiation (Tonboe et al. 2005).

1.3 The Algorithm

The ASI algorithm is a hybrid of two sea ice concentration algorithms (Kaleschke et al. 2001, Spreen et al 2008). The first is that proposed by Svendsen et al. (1987) for frequencies near 90 GHz and the second is the Bootstrap algorithm (Comiso 1995). The Bootstrap algorithm is only used where no ice is present. The ASI algorithm processes 89 GHz brightness temperature from the Advanced Microwave Scanning Radiometer (AMSR-2) sensor mounted on the Global Change Observation Mission -Water (GCOM-W1) satellite.

In the Svendsen algorithm, the concentrations of ice and water are defined such that

$$1 = C_W + C_F + C_M, \quad (2)$$

| Case | 95 th percentile discrepancy | Date (2015) | Latitudes | Longitudes |
|------|---|--------------|-----------------|-----------------|
| 1 | 32.34% | 24 March | 73.00 - 73.70 N | 120.5 - 124.0 E |
| 2 | 20.45% | 8 March | 67.00 - 69.00 N | 115.0 - 107.0 W |
| 3 | 26.58% | 27 March | 75.00 - 76.50 N | 115.0 - 107.0 W |
| 4 | 20.32% | 24 April | 70.20 - 71.00 N | 152.4 - 150.1 W |
| 5 | 30.20% | 15 March | 70.50 - 72.75 N | 129.7 - 135.0 E |
| 6 | 4.01% | 2 February | 70.10 - 70.25 N | 159.5 - 162.0 E |
| 7 | 7.29% | 1 January | 70.80 - 71.40 N | 152.4 - 159.0 E |
| 8 | 6.98% | February 2nd | 82.40 - 83.60 N | 56.0 - 48.0 W |
| 9 | 14.92% | March 13th | 69.20 - 72.50 N | 100.0 - 98.4 W |
| 10 | 2.39% | February 2nd | 67.70 - 70.30 N | 68.9 - 66.2 W |

Table 1.1.1: An overview of the cases. The 95th percentile maximum discrepancy was calculated by first finding the maximum error for each case and day (assuming 100% is correct for landfast ice) and then calculating the 95th percentile of those maximum errors. The values and dates in the table are from the days on which the maximum error was closest to that calculated as the 95th percentile. Only dates from January through April of 2015 were used in this calculation, and January was omitted from cases 6, 8, and 10 due to difficulties verifying actual ice concentration.

where C_W represents the concentration of water, C_F represents the concentration of first-year ice, and C_M represents the concentration of multi-year ice (ice that is more than a year old). Due to the similarities in their polarization differences, which are used to find concentration, C_F and C_M are combined in the variable C_{ice} . Since the emissivity of each substance is proportional to its concentration, it follows that

$$T_{B,total} = C_W T_{B,water} + C_{ice} T_{B,ice}, \quad (3)$$

where T_B is brightness temperature.

Since the received polarization difference is a weighted fraction of the polarization differences of water and ice, based on concentration, Equation (3) can be written as

$$P = C_W P_W + C_{ice} P_{ice}. \quad (4)$$

Incorporating atmospheric effects and combining equations (2) and (4), Svendsen et al. (1987) proposes the equation

$$C_T = d_3 P^3 + d_2 P^2 + d_1 P + d_0, \quad (5)$$

which is basis of the ASI algorithm for areas where ice is present. The incorporation of atmospheric effects into the algorithm is discussed in more detail in Section 2.3.

Due to the high sensitivity to water vapor near 90 GHz, three weather filters are incorporated. The concentrations at all points which these filters determine to be ice-free are set to 0 (Kaleschke et al. 200, Spreen et al. 2008). Two gradient ratio filters and a filter based on an independent, low-frequency sea ice concentration algorithm are used (Spreen et al. 2008).

The gradient ratio of two frequencies M and N is defined based on the vertical polarization of brightness temperature ($T_{B,V}$) as

$$GR(M, N) = \frac{T_{B,V}(M) - T_{B,V}(N)}{T_{B,V}(M) + T_{B,V}(N)}. \quad (6)$$

The sea ice concentration in the ASI algorithm is set to 0 where $GR(36.5, 18.7)$ is greater than or equal to 0.045 or $GR(23.8, 18.7)$ is greater than or equal to 0.04. The third filter sets the concentrations at all points found to have no ice by the Bootstrap algorithm (another concentration algorithm) to 0 (Spreen et al. 2008).

2. DATA AND METHODS

2.1 Data

This study uses three types of data. The first type is 89 GHz polarized brightness temperature from the Advanced Microwave Scanning Radiometer (AMSR-2) sensor mounted on the Global Change Observation Mission - Water (GCOM-W1) satellite operated by the Japanese Aerospace Exploration Agency (JAXA) and provided by the University of Bremen (see AMSR-2 in References). The daily averages of the brightness temperatures have been gridded to a 6.25 km resolution polar stereographic grid.

The second data source is the output of the ASI algorithm using the gridded brightness temperatures from AMSR-2 as input. This data is likewise available on a 6.25 km polar stereographic grid and was provided by the University of Bremen.

The last type of data used is the European Centre for Medium-Range Weather Forecasting (ECMWF) ERA-Interim Reanalysis dataset (Dee et al., 2011). For this study, the 0.4° resolution was used. This means that there was a data point every 0.4° longitude and every 0.4° latitude. 2 m temperature, ice surface temperature, snow depth, total column water, total column ozone, top net thermal radiation, surface net thermal radiation, surface latent heat flux, and a land

mask were used from this dataset. The surface roughness and forecast surface roughness parameters provided was examined, but not used due to suspected inaccuracy over sea ice.

2.2 Methods

First, several potential causes of the anomalies in cases 1, 2, 3, 4, 5, and 9 were identified based on physical reasoning. For each potential cause, key parameters were plotted in timeseries and/or correlation plots with either polarization difference or ASI C_{ice} . The timeseries plots were analyzed visually for patterns and correlation coefficients and p-values were found for all correlation plots.

3. Potential Causes

3.1 Temperature

Temperature could have affected the brightness temperatures recorded by AMSR-2 in several ways. The most obvious reason would be that the temperature occasionally rose above zero degrees Celsius and caused the surface of the ice to melt or caused the snow on top of the ice to melt and re-freeze as a specular, strongly polarizing interface. This effect would be similar for any instance causing water to appear on the ice. Water on top of ice appears the same as open water to the AMSR-2 sensor. Either of these would cause brightness temperature polarization to increase while leaving the underlying ice intact.

Another reason to suspect temperature as a potential cause is the well-known dependence of emissivity on temperature. If temperature had affected horizontal and vertical emissivities of the ice unequally, it would have changed the polarization difference received by AMSR-2 and thus the output of the ASI algorithm.

Temperature is not the only factor which affects brightness temperature, so other factors could still be responsible.

3.2 Surface Roughness

Surface roughness is widely known to have a significant effect on brightness temperature (Shokr and Sinha 2015, Grenfell et al. 1988), although its quantification is inconsistent. It can be characterized qualitatively, as in Grenfell et al. (1988), or by the correlation length or root mean square (rms) height (Manninen 1997). Grenfell et al. (1988) showed that the effect of surface roughness on brightness temperature does not necessarily change both polarizations by the same amount around 89 GHz. Therefore, it seems reasonable that unusual surface roughness could have caused the anomalies.

3.3 Snow

Snow can scatter radiation and thus decrease the polarization difference (Tonboe et al. 2005). It also affects surface roughness. Therefore, snow depth could be a cause. Because the dense layer of snow affects polarization difference the most (Tonboe et al. 2005), another possibility would be that the snow was present and deep, but had low density.

3.4 Atmospheric Interference

Scattering does not only occur in the snow layer, but also in the atmosphere. Both the intensity and polarization of radiation can change between the ground and the satellite. The 89 GHz channel used by the ASI algorithm is especially prone to interference from water vapor. In the algorithm, the change in polarization is accounted for by the equation

$$P_{received} = P_{surface} \alpha. \quad (7)$$

In this equation, α is defined as

$$\alpha = e^{-\tau}(1.1e^{-\tau} - 0.11) \quad (8)$$

where τ represents atmospheric opacity and is considered to be constant (Spreen et al. 2008). Combining equations (5), (7), and (8), it is found that

$$C_{ASI} = \frac{x}{e^{-3\tau}(1.1e^{-\tau}-0.11)^3} P_{received}^3 + \frac{y}{e^{-2\tau}(1.1e^{-\tau}-0.11)^2} P_{received}^2 + \frac{z}{e^{-\tau}(1.1e^{-\tau}-0.11)} P_{received} + d_0. \quad (9)$$

In this equation, x , y , and z are some constant coefficients. The coefficient d from Equation (5) is not used because α is used to calculate d . The assumption that α is a smooth function of C used to find Equation (5) does not account for any factors which influence α other than that there is generally more water vapor over open water than over ice. Since atmospheric opacity is influenced by more factors than just ice concentration, this could be a source of error. Because x and z are both small and y is large and negative, Equation (9) shows that if τ is underestimated, C would be overestimated.

Figure 3.4.1 shows a case where the presence of water vapor caused an overestimation of sea ice concentration.

3.5 Radiation

Latent heat could cause melting, even if the temperature were below freezing. In the case of sea ice, radiative flux could be this source of latent heat. Any melting could cause liquid water to form on top of the ice or create a strongly polarizing ice crust which would cause the ASI algorithm to underreport C_{ice} .

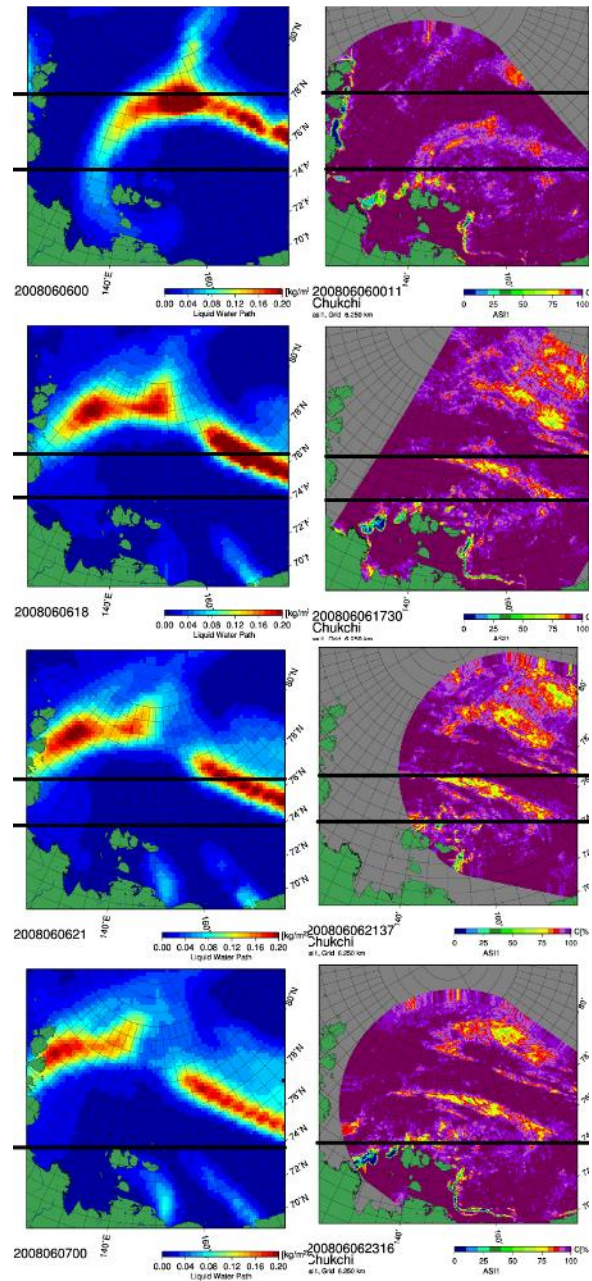


Figure 3.4.1: Images courtesy of Junshen Lu and generated using ECMWF ERA Interim data (Dee et al., 2011) and AMSR-2 sea ice concentration generated using the ASI algorithm. Images on the left show total column water in km/m^2 , where red is 0.2 and dark blue is 0, and images on the right show sea ice concentration in percent. The pairs of images are three hours apart from each other.

3.6 Grain Size and Wind Crusts

As snow is altered by wind, the grain sizes at the surface increase. The resulting layer of large grains, called a wind crust, can significantly affect the horizontal polarization of brightness temperature (Stogryn 1986). The Snow Grain Size and Pollution amount (SGSP) retrieval based on microwave data collected by the MODIS satellites additionally overestimates the grain size by 23 to 77% if a wind crust is present (Wiebe 2011). Therefore, a strong correlation between grain size reported by the SGSP algorithm and polarization difference would be expected if a wind crust were responsible.

3.7 Salinity

Many, but not all, of the cases investigated have low salinity according to model data (Figure 3.7.1), which was used because of the dearth of observational data. However, salinity of sea ice can also be affected by environmental conditions as the ice forms. In addition, the Arctic Cap Nowcast/Forecast System (ACNFS) model used does not seem to have published validation of salinity in polar regions. Because of the lack of validation and of data to input, the model may have a large error and the influence of salinity would need to be tested using another data set.

4. RESULTS

4.1 Temperature

Ice formation is typically considered to begin when temperatures have continuously

ARCC0.08-04.1 Sea surface salinity (psu): 20151002

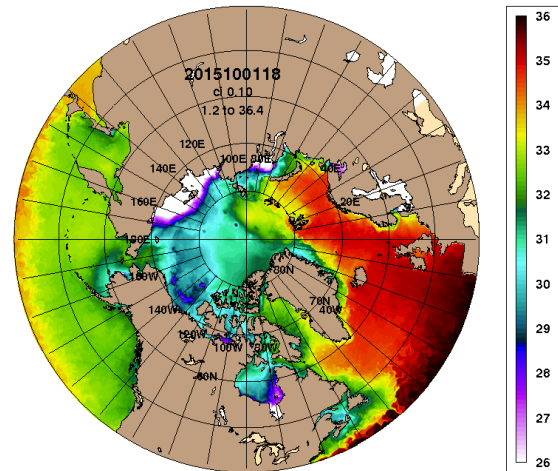


Figure 3.7.1: Image of ACNFS model output for October 2, 2015 from initialization on October 1. Salinity in Practical Salinity Units (psu). Obtained from https://www7320.nrlssc.navy.mil/hycomARC/navo/arclist_arcticsss.html

been below -1.8 degrees Celsius, the freezing point of most ocean water, for five days. Because salt is ejected from the ice as it forms (Shokr and Sinah 2015, Cox and Weeks 1974), ice is significantly less saline than the water it forms from and thus melts at approximately 0 degrees Celsius. To test the hypothesis that melting due to temperature change was responsible for the anomalies, the average 2 m air temperature for each case was plotted as timeseries (Figure 4.1.1). The average temperature for each anomaly area only rose above freezing after the ice formation start date (marked with a blue line) and before late Spring in 2 of the 10 cases. Only one of these cases has an anomaly. Therefore, the melting and refreezing of ice or snow cannot be the cause of these anomalies. The possibility that the rate of freeze causes

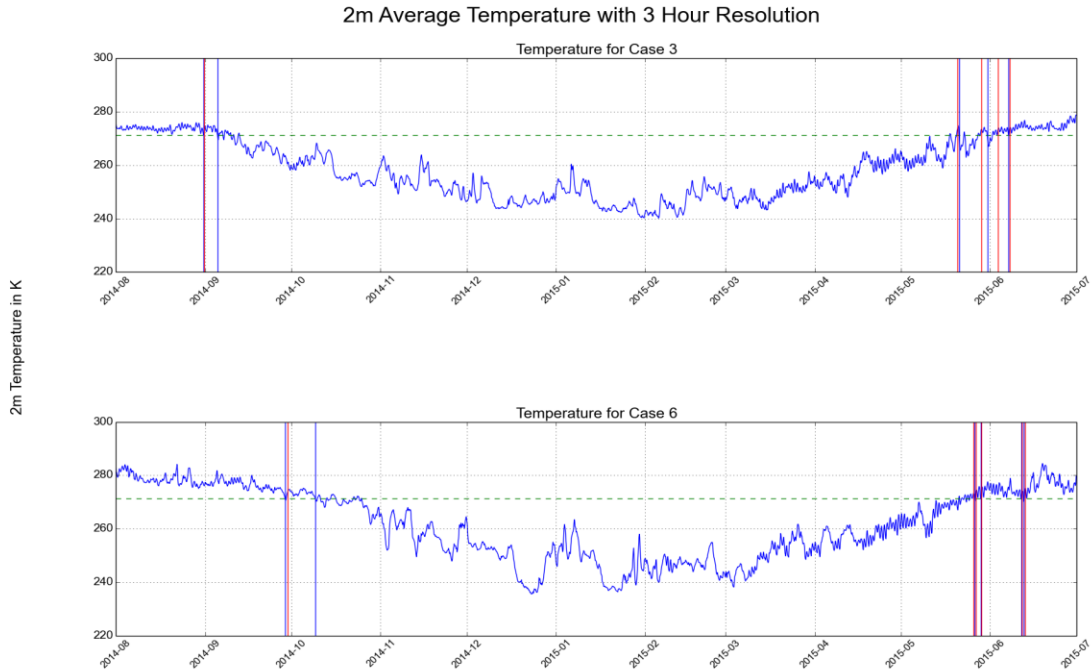


Figure 4.1.1: The average 2m temperatures over Cases 3 (top) and 6 (bottom) beginning 1 August 2015. The anomaly area for Case 6 was expanded by 0.5° in each direction due to data resolution. Data comes from the ERA Interim reanalysis dataset provided by ECMWF. Red lines denote days when the temperature rose above 0°C after ice formation. Blue lines denote the start of ice formation, when the temperature has remained below -1.8°C for five consecutive days. Similar plots for all cases can be found in Appendix B.

the anomalies can also be eliminated by observing the span of blue and red lines during the freeze season.

The hypothesis that temperature affected the emissivities differently was tested as a potential cause both visually, by plotting polarization difference and sea ice temperature in timeseries, and mathematically, by calculating the correlation coefficient of sea ice temperature and polarization difference for each case. The plots created clearly show that there is not a simple relationship between temperature and polarization (Figures 4.1.2 and 4.1.3). The strength of correlation between the two quantities also appears to be unrelated to how well the algorithm performed.

Figure 4.1.2: Timeseries of ice surface temperature and polarization difference for Case 2 from January through April of 2015.

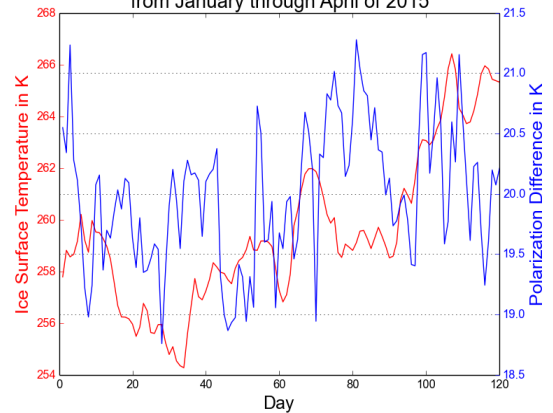


Figure 4.1.2: Timeseries of ice surface temperature (red) from ERA Interim reanalysis data and polarization difference (blue) calculated from the AMSR-2 brightness temperature products for January through April of Case 2. Note that polarization difference is inversely related to the output of the ASI algorithm due to the large, negative value of d_2 in Equation (5).

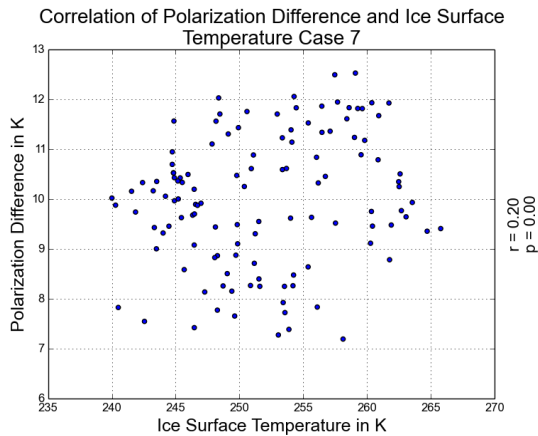


Figure 4.1.3: Correlation of ice surface temperature from ERA Interim reanalysis data and polarization difference calculated from the AMSR-2 brightness temperature products for January through April of Case 7. Correlation coefficients ranged from 0.07 in Case 4 to 0.41 in Case 3 with no apparent relation to the performance of the algorithm. More details can be found in Appendix C.

4.2 Snow Depth

The first snow-related hypothesis tested in this study was that the depth of the snow was related to the strength of the anomaly. If this were true, we would expect lower snow depth on the days when the anomalies were most intense. Figure 4.3.1 shows the timeseries generated to test this hypothesis. Due to the difficulty retrieving

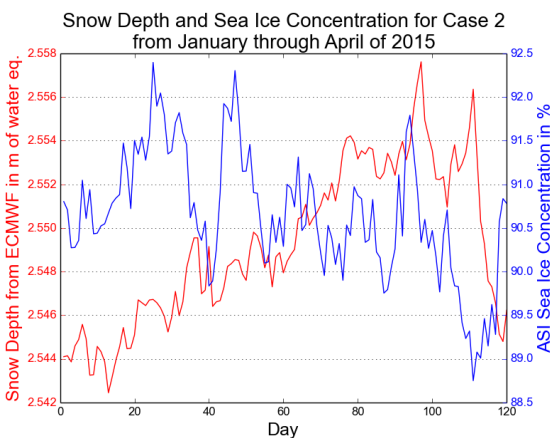


Figure 4.2.1: Timeseries of snow depth from ERA-Interim Reanalysis data on adjacent land and sea ice concentration from the ASI algorithm

snow depth from ice with current remote sensing methods, snow depth data for the adjacent land were used. While this creates a potentially large source of error, the general trend of increasing snow depth throughout the winter should hold. The diagram shows that snow depth generally increases while the anomaly varies, so snow depth is not a likely cause of the anomalies.

4.3 Water Vapor and Ozone

One of the correlation plots generated to investigate the influence of water vapor in the cases under investigation is shown in Figure 4.3.1. The lack of correlation suggests that interference from water vapor is not the cause of the anomalies. The same type of investigation was made for total column ozone with similar results.

4.4 Radiation

To investigate the role of radiative flux in the anomalies, the correlation coefficients of several radiation products from ECMWF ERA-Interim reanalysis dataset and polarization difference were

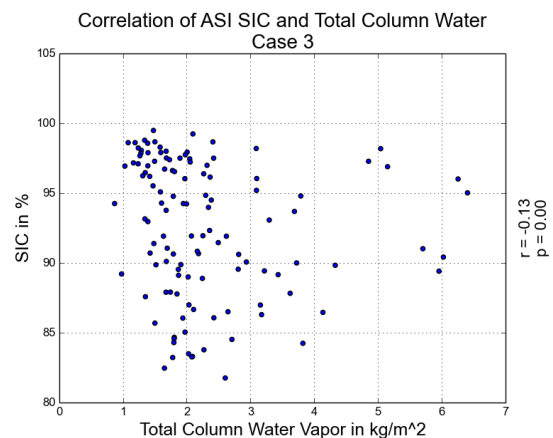


Figure 4.3.1: Correlation of sea ice concentration from the ASI algorithm with total column water vapor from the ERA-Interim Reanalysis dataset for January through April 2015 of Case 3.

calculated from January through April for all cases. These quantities included surface latent heat flux, surface net thermal radiation, and top net thermal radiation. No correlation coefficients with magnitude greater than 0.44 (Appendix C) were found, and the quantity with the highest correlation was top net thermal radiation. This is expected due to the relatively high (0.41) correlation coefficient of surface temperature and sea ice concentration found for the same case (Appendix C). Based on these results, it is unlikely that radiative flux is the cause of the anomalies.

4.5 Snow Grain Size

To test the hypothesis that wind or another type of crust caused the observed anomalies, the SGSP algorithm was run for each case for the month of April in 2015. This data was divided into two data sets. The first set contains data from the first half of April, and the second data set contains data from the second half. The average snow grain size for each case and data set (using the boundaries define in Table 1.1.1) was then calculated, resulting in 20 data points.

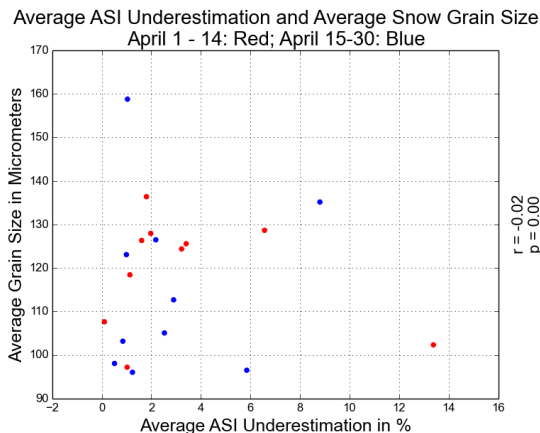


Figure 2.6.1: Average grain size per case according to the SGSP algorithm and the average concentration underestimation of the ASI algorithm for the first and second halves of April, 2015. A land mask was used for ASI concentration but not for snow grain size.

The snow grain size was not landmasked and it was assumed that snow grain size for the top layer over ice and the adjacent land are similar. Corresponding averages of ASI concentration underestimation were calculated using a landmask. The correlation was then plotted and showed that neither a wind crust nor snow grain size was the cause of the anomalies (Figure 2.6.1).

4.6 Untestable Causes

The possibilities that surface roughness, snow density, atmospheric constituents besides water vapor and ozone, or salinity had a role in the creation of the anomalies could not be tested due to lack of data. More data may be available in the future to be analyzed in future studies.

5. CONCLUSION

This study found that the ASI algorithm significantly underestimates sea ice concentration in several landfast ice cases, but performs well in others. Surface roughness, snow properties, and salinity may be capable of causing the algorithm to underreport. Temperature, snow grain size, radiative flux, crusting, and some factors of atmospheric interference were tested and found not to be the cause of the anomalies investigated. Due to lack of data availability, the effects of surface roughness, salinity, snow density profiles, and atmospheric constituents besides water and ozone could not be tested. The possibility of polarizing atmospheric interference was also not considered. All correlation coefficients and p-values calculated excluding those for snow grain size (because the correlation was calculated using all cases) can be found in Appendix C.

It is important to find the cause of these anomalies in order to add corrections

to the ASI algorithm. As more data becomes available, potential factors left unexplored in this study should be investigated. However, these underestimations do not mean that the algorithm is bad, though it should be treated with care in areas with fast ice. It is still a good source of high-resolution sea ice concentration in most instances.

6. ACKNOWLEDGMENTS

Thanks to Junshen Lu for information about other cases in which the ASI algorithm underestimated sea ice concentration due to water vapor, Dr. Marcus Huntemann for help understanding the physics behind the polarization of brightness temperature, Dr. Larysa Istomina for assistance with the SGSP processing chain, and to the entire Remote Sensing of Polar Regions group at the Institute for Environmental Physics.

This work was funded by the Research Internships in Science and Engineering program of the German Academic Exchange Service (DAAD-RISE).

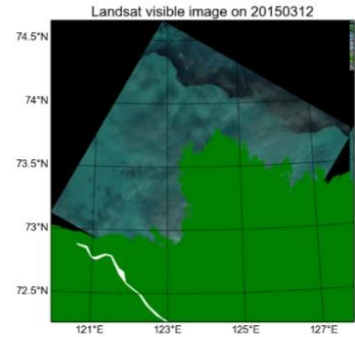
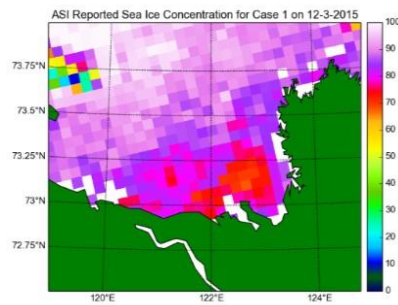
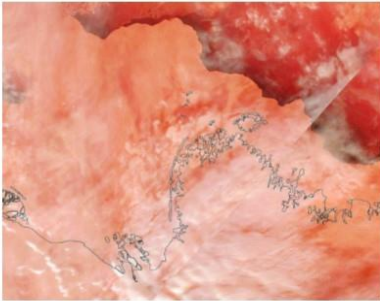
7. REFERENCES

- AMSR-2 Brightness Temperature from the Japan Aerospace Exploration Agency provided by the University of Bremen, accessed May 2017, available at seaice.uni-bremen.de.
- Comiso, J. C., 1995: SSM/I Sea Ice Concentration Using the Bootstrap Algorithm. *NASA Reference Publication*, **1380**.
- Cox, G. F. N., and W. F. Weeks, 1974: Salinity Variations in Sea Ice. *Journal of Glaciology*, **13**, 67, 109-120.
- Dee, D. P., and Coauthors (2011), The ERA Interim reanalysis: configuration and performance of the data assimilation system. *Q.J.R. Meteor. Soc.*, 137: 553–597. doi: 10.1002/qj.828.
- European Centre for Medium-Range Weather Forecasts, 2015: Cycle 41r1 detailed description of the upgrade. Accessed 12 July 2017. [Available online at https://www.ecmwf.int/en/forecasts/documentation-and-support/changes-ecmwf-model/cycle-41r1#meteorological_changes.]
- European Centre for Medium-Range Weather Forecasts, 2016: Set I – Atmospheric Model high resolution 10-day forecast (HRES). Accessed 12 July 2017. [Available online at <https://www.ecmwf.int/en/forecasts/data/sets/set-i>.]
- Grenfell, T. C., D. L. Bell, A. W. Lohanick, C. T. Swift, and K. St. Germain, 1988: Multifrequency passive microwave observation of saline ice grown in a tank. *Remote Sensing: Moving Toward the 21st Century*, 1687-1690.
- Kaleschke, L., C. Lüpkes, T. Vihma, J. Haarpainter, A. Bochert, J. Hartman, and G. Heygster, 2001: SSM/I Sea Ice Remote Sensing for Mesoscale Ocean-Atmosphere Interaction Analysis. *Canadian Journal of Remote Sensing*, **27**, 5, 526:537, doi: 10.1080/07038992.2001.10854892.

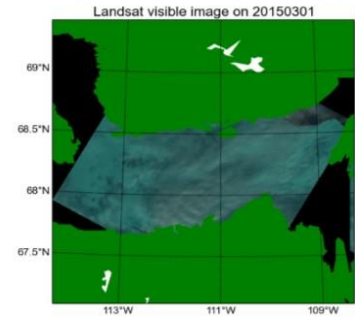
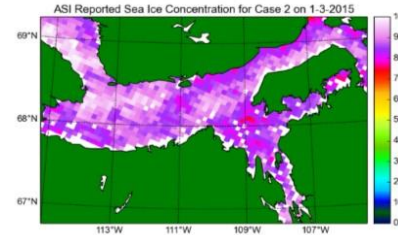
- Lee, S. M., and B. J. Sohn, 2015: Retrieving the refractive index, emissivity, and surface temperature of polar sea ice from 6.9 GHz microwave measurements: A theoretical development. *Journal of Geophysical Research: Atmospheres*, **120**, 2293-2305, doi: 10.1002/2014JD022481.
- Manninen, A. T., 1997: Surface roughness of Baltic sea ice. *Journal of Geophysical Research*, **102**, C1, 1119-1139.
- Shokr, M., and N. K. Sinha, 2015: Ice Physics and Physical Processes. *Sea Ice Physics and Remote Sensing*, John Wiley & Sons, Inc., 27-98 and 379-380.
- Svendsen, Einar, Christian Mätzler, and Thomas C. Grenfell, 1987: A model for retrieving total sea ice concentration from a spaceborne dual-polarized passive microwave instrument operating near 90 GHz. *International Journal of Remote Sensing*, **8**, 10, 1479-1487, doi: 10.1080/01431168708954790.
- Spren, G., L. Kaleschke, and G. Heygster, 2008: Sea ice remote sensing using AMSR-E 89-GHz channels. *Journal of Geophysical Research*, **113**, doi: 10.1029/2005JC003384.
- Stogryn, A., 1986: A Study of the Microwave Brightness Temperature of Snow from the Point of View of Strong Fluctuation Theory. *IEEE Transactions on Geoscience and Remote Sensing*, **GE-24**, 2.
- Tonboe, R., S. G. Heygster, L. T. Pedersen, and S. Andersen, 2005: Surface Emission, *Thermal Microwave Radiation: Applications for Remote Sensing*, C. Mätzler, Ed., The Institution of Engineering and Technology, 382-425.
- Wiebe, H., 2007: Validation of the ARTIST Sea Ice (ASI) Concentration Algorithm and Geolocation of the Microwave Radiometer AMSR-E data. Master Thesis, Institute of Environmental Physics, University of Bremen, 84 pp.
- Wiebe, H., 2011: Implementation and validation of the snow grain size retrieval SGSP from spectral reflectances of the satellite sensor MODIS. PhD thesis, Institute of Environmental Physics, University of Bremen, 106 pp.

APPENDIX A: MODIS visible imagery, ASI algorithm concentration, and Landsat visible imagery for one selected day of each case. Note molted coloring is due to clouds.

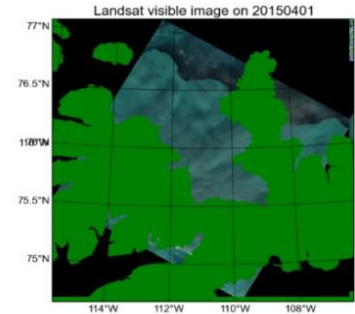
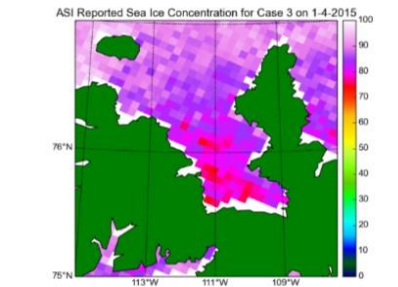
MODIS visible channels 3-6-7



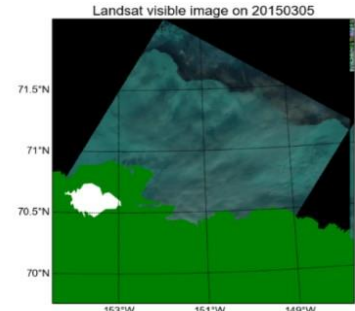
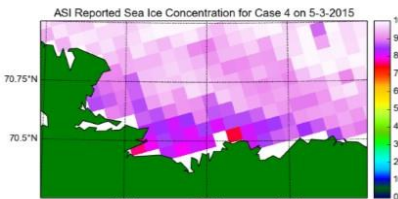
MODIS visible channels 3-6-7



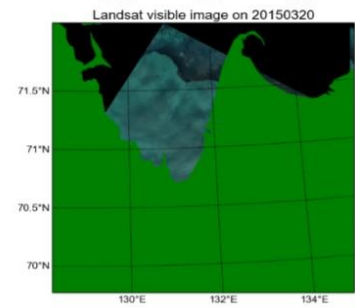
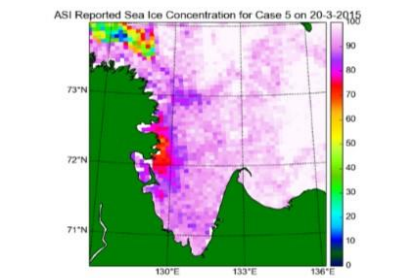
MODIS visible channels 3-6-7



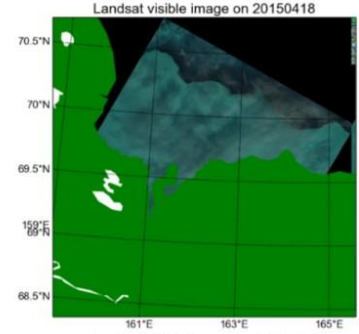
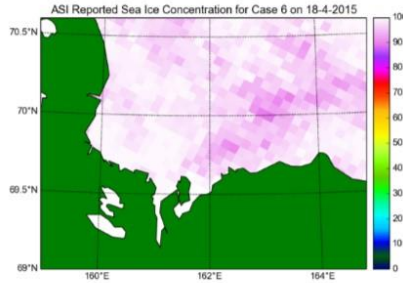
MODIS visible true color



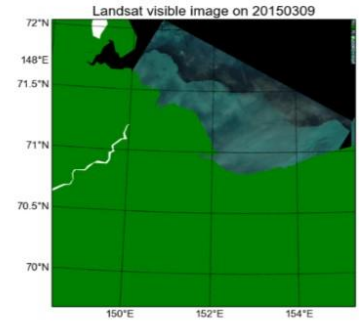
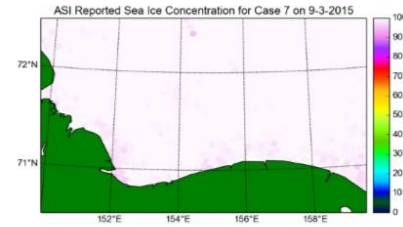
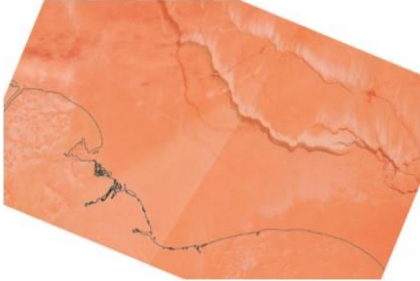
MODIS visible true color



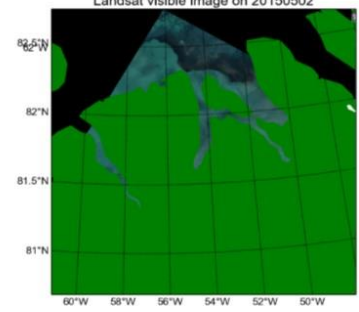
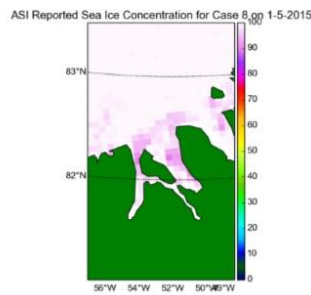
MODIS visible channels 3-6-7



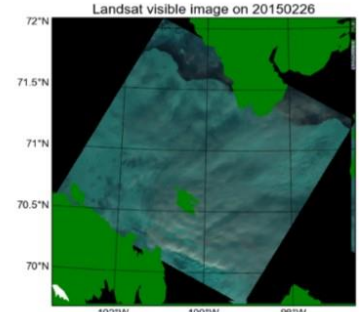
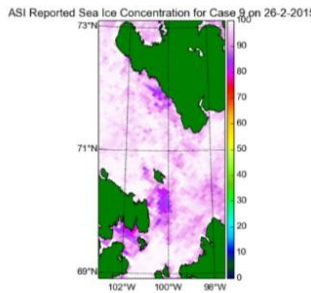
MODIS visible channels 3-6-7



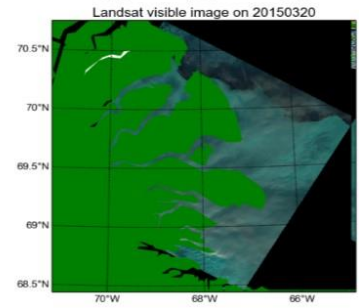
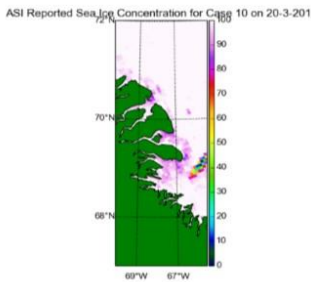
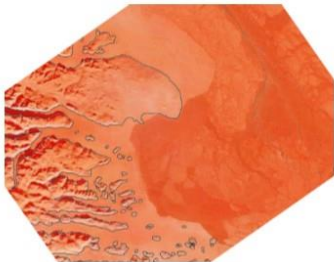
MODIS visible channels 3-6-7



MODIS visible channels 3-6-7

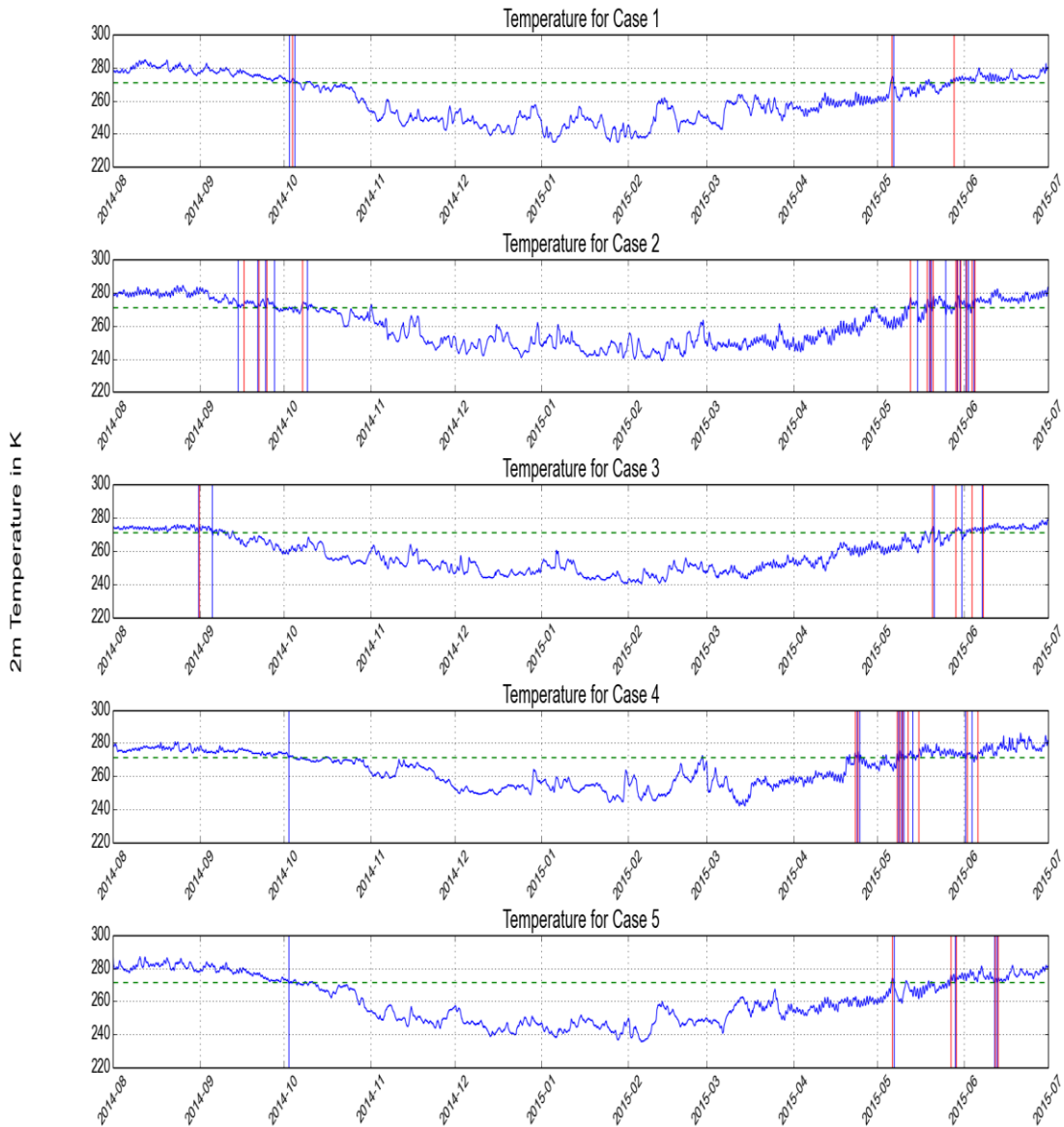


MODIS visible channels 3-6-7

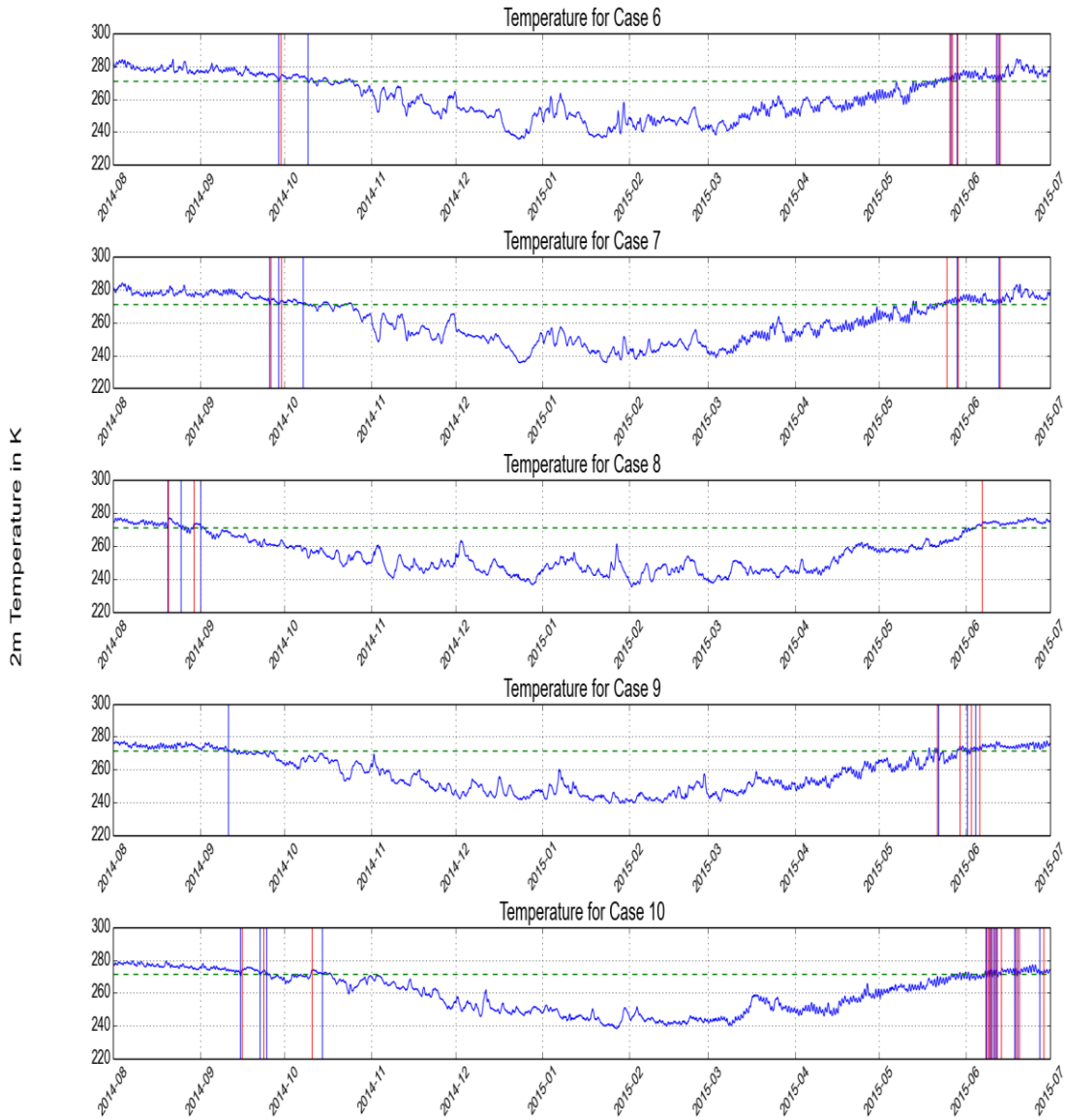


APPENDIX B: The average 2m temperatures for all cases beginning August 1st. The anomaly area for Case 6 was expanded by 0.5° in each direction due to data resolution. Data comes from the ERA Interim reanalysis dataset provided by the European Centre for Medium-Range Weather Forecasting (ECMWF) (Dee et al. 2011). Red lines denote days when the temperature rose above 0°C after ice formation. Blue lines denote the start of ice formation, when the temperature has remained below -1.8°C for five consecutive days. The possibility that the rate of freeze causes the anomalies can be eliminated by observing the span of blue and red lines during the freeze season.

2m Average Temperature with 3 Hour Resolution



2m Average Temperature with 3 Hour Resolution



APPENDIX C: Correlation Coefficients and P-Values of several quantities with the output of the ASI concentration algorithm for each case.

Case 1:

| Variable | Correlation Coefficient | P-Value |
|-------------------------------|-------------------------|---------|
| Ice Surface Temperature | -0.354 | 0.000 |
| Total Column Water | -0.193 | 0.000 |
| Estimated Snow Depth | 0.441 | 0.000 |
| Surface Latent Heat Flux | -0.108 | 0.001 |
| Surface Net Thermal Radiation | -0.317 | 0.000 |
| Top Net Thermal Radiation | -0.115 | 0.000 |

Case 2:

| Variable | Correlation Coefficient | P-Value |
|-------------------------------|-------------------------|---------|
| Ice Surface Temperature | 0.282 | 0.000 |
| Total Column Water | 0.368 | 0.000 |
| Estimated Snow Depth | -0.469 | 0.000 |
| Surface Latent Heat Flux | 0.042 | 0.006 |
| Surface Net Thermal Radiation | 0.004 | 0.000 |
| Top Net Thermal Radiation | -0.394 | 0.000 |

Case 3:

| Variable | Correlation Coefficient | P-Value |
|-------------------------------|-------------------------|---------|
| Ice Surface Temperature | -0.455 | 0.000 |
| Total Column Water | -0.125 | 0.000 |
| Estimated Snow Depth | -0.740 | 0.000 |
| Surface Latent Heat Flux | -0.038 | 0.027 |
| Surface Net Thermal Radiation | 0.245 | 0.000 |
| Top Net Thermal Radiation | 0.447 | 0.000 |

Case 4:

| Variable | Correlation Coefficient | P-Value |
|-------------------------------|-------------------------|---------|
| Ice Surface Temperature | -0.228 | 0.000 |
| Total Column Water | -0.127 | 0.000 |
| Estimated Snow Depth | -0.276 | 0.000 |
| Surface Latent Heat Flux | -0.003 | 0.001 |
| Surface Net Thermal Radiation | 0.104 | 0.000 |
| Top Net Thermal Radiation | -0.013 | 0.000 |

Case 5 (longitude increased by 0.1° in each direction due to data resolution):

| Variable | Correlation Coefficient | P-Value |
|-------------------------------|-------------------------|---------|
| Ice Surface Temperature | -0.417 | 0.000 |
| Total Column Water | -0.324 | 0.000 |
| Estimated Snow Depth | 0.214 | 0.000 |
| Surface Latent Heat Flux | -0.021 | 0.063 |
| Surface Net Thermal Radiation | 0.047 | 0.000 |
| Top Net Thermal Radiation | 0.162 | 0.000 |

Case 6 (latitude increased by 0.1° in each direction due to data resolution):

| Variable | Correlation Coefficient | P-Value |
|-------------------------------|-------------------------|---------|
| Ice Surface Temperature | 0.026 | 0.000 |
| Total Column Water | -0.010 | 0.000 |
| Estimated Snow Depth | 0.249 | 0.000 |
| Surface Latent Heat Flux | 0.006 | 0.130 |
| Surface Net Thermal Radiation | 0.043 | 0.000 |
| Top Net Thermal Radiation | -0.062 | 0.000 |

Case 7:

| Variable | Correlation Coefficient | P-Value |
|-------------------------------|-------------------------|---------|
| Ice Surface Temperature | -0.364 | 0.000 |
| Total Column Water | -0.104 | 0.000 |
| Estimated Snow Depth | 0.175 | 0.000 |
| Surface Latent Heat Flux | 0.014 | 0.185 |
| Surface Net Thermal Radiation | -0.041 | 0.000 |
| Top Net Thermal Radiation | 0.154 | 0.000 |

Case 8:

| Variable | Correlation Coefficient | P-Value |
|-------------------------------|-------------------------|---------|
| Ice Surface Temperature | -0.393 | 0.000 |
| Total Column Water | -0.313 | 0.000 |
| Estimated Snow Depth | 0.052 | 0.000 |
| Surface Latent Heat Flux | -0.034 | 0.137 |
| Surface Net Thermal Radiation | -0.006 | 0.000 |
| Top Net Thermal Radiation | 0.240 | 0.000 |

Case 9:

| Variable | Correlation Coefficient | P-Value |
|-------------------------------|-------------------------|---------|
| Ice Surface Temperature | -0.210 | 0.000 |
| Total Column Water | 0.112 | 0.000 |
| Estimated Snow Depth | -.0482 | 0.000 |
| Surface Latent Heat Flux | -0.098 | 0.017 |
| Surface Net Thermal Radiation | -0.082 | 0.000 |
| Top Net Thermal Radiation | 0.102 | 0.000 |

Case 10:

| Variable | Correlation Coefficient | P-Value |
|-------------------------------|-------------------------|---------|
| Ice Surface Temperature | -0.133 | 0.000 |
| Total Column Water | 0.012 | 0.000 |
| Estimated Snow Depth | -0.016 | 0.000 |
| Surface Latent Heat Flux | -0.005 | 0.006 |
| Surface Net Thermal Radiation | -0.075 | 0.000 |
| Top Net Thermal Radiation | 0.011 | 0.000 |